Physics of the Earth and Planetary Interiors 333 (2022) 106944

Contents lists available at ScienceDirect

Physics of the Earth and Planetary Interiors

journal homepage: www.elsevier.com/locate/pepi

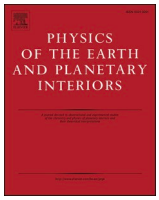

The role of slow magnetostrophic waves in the formation of the axial dipole in planetary dynamos

Aditya Varma , Binod Sreenivasan *

Centre for Earth Sciences, Indian Institute of Science, Bangalore 560012, India

ARTICLE INFO

Keywords:
Planetary dynamos
Axial dipole field
Magnetostrophic waves

ABSTRACT

The preference for the axial dipole in planetary dynamos is investigated through the analysis of wave motions in spherical dynamo models. Our study focuses on the role of slow magnetostrophic waves, which are generated from localized balances between the Lorentz, Coriolis and buoyancy (MAC) forces. Since the slow waves are known to intensify with increasing field strength, simulations in which the field grows from a small seed towards saturation are useful in understanding the role of these waves in dynamo action. Axial group velocity measurements in the energy-containing scales show that fast inertial waves slightly modified by the magnetic field and buoyancy are dominant under weak fields. However, the dominance of the slow waves is evident for strong fields satisfying $|\omega_M/\omega_C| \sim 0.1$, where ω_M and ω_C are the frequencies of the Alfvén and inertial waves respectively. A MAC wave window of azimuthal wavenumbers is identified in which helicity generation by the slow waves strongly correlates with dipole generation. Analysis of the magnetic induction equation suggests a poloidal–poloidal field conversion in the formation of the dipole. Finally, the attenuation of slow waves may result in polarity reversals in a strongly driven Earth's core.

1. Introduction

Planetary dynamos are driven by thermochemical convection in their fluid cores. The axial dipole dominates a large region of the parameter space in convection-driven dynamos where the effect of planetary rotation, measured by the Coriolis forces, is large relative to that of both nonlinear inertia and viscosity (Sreenivasan and Jones, 2006; Schaeffer et al., 2017). Rapid rotation produces anisotropic convection with equatorially antisymmetric axial motions, the helicity of which is thought to be essential for dynamo action (Moffatt, 1978). A long-standing question in planetary dynamo theory is whether the preference for the axial dipole is due to a purely hydrodynamic process influenced by rotation or due to a magnetohydrodynamic process influenced by both rotation and the self-generated magnetic field. Answering this question would also help us constrain the parameter space that admits polarity reversals in strongly driven dynamos (e.g. Sreenivasan et al., 2014).

An early study by Busse (1976) used the linear theory of magnetoconvection to explore the onset of dynamo action in an annulus. Busse found that the effect of a magnetic field on convection enhanced magnetic field generation. This interesting idea was explored further by Sreenivasan and Jones (2011) who showed that the presence of a magnetic field substantially enhanced the kinetic helicity of columnar convection. They considered linear magnetoconvection in a spherical shell in the rapidly rotating limit $E \to 0$, where E is the Ekman number that gives the ratio of viscous to Coriolis forces. Although the spatially varying magnetic field in a nonlinear dynamo does not substantially lower the threshold for convective onset relative to that in the nonmagnetic system, a substantial enhancement of helical convection occurs in the neighbourhood of the length scale of energy injection (Sreenivasan and Kar, 2018). The growth of convection is notably absent in a kinematic dynamo, which fails to produce the axial dipole with the same parameters and initial conditions. While nonlinear dynamo models strongly relate field-induced helicity generation in the energy-containing scales to dipole formation, the primary force balance in these scales is known to be approximately geostrophic (Aurnou and King, 2017; Aubert et al., 2017), which raises the question of how the field acts on these scales so as to enhance helicity. The present study addresses this question by analyzing wave motions in the energy-containing scales in planetary dynamo models.

Wave motions in planetary cores arise from the effects of rotation, magnetic field and buoyancy. Torsional oscillations propagating radially

* Corresponding author.
E-mail address: bsreeni@iisc.ac.in (B. Sreenivasan).

https://doi.org/10.1016/j.pepi.2022.106944
Received 16 February 2022; Received in revised form 22 September 2022; Accepted 22 September 2022
Available online 28 September 2022
0031-9201/© 2022 Elsevier B.V. All rights reserved.

at the Alfvén speed across concentric cylinders have been simulated in low-inertia numerical models of the geodynamo (Wicht and Christensen, 2010; Teed et al., 2014). Non-axisymmetric Alfvén waves propagating along the cylindrical radius are conceivable (Jault, 2008; Bardsley and Davidson, 2016; Aubert and Finlay, 2019) since the convection is made up of thin columns aligned with the rotation axis. Slow Magneto-Coriolis (MC) Rossby waves, thought to produce the westward drift of the Earth's magnetic field, have been realized in dynamo simulations (Hori et al., 2015). While convection can onset in the form of Alfvén waves in a non-rotating Bénard layer (Roberts and Zhang, 2000), the planetary regime of strong rotation can support convection through fast and slow Magnetic-Archimedean-Coriolis (MAC) waves. The fast MAC waves are inertial waves weakly modified by the magnetic field and buoyancy; the slow MAC, or magnetostrophic, waves are slow MC waves modified by buoyancy (Braginsky, 1967; Busse et al., 2007). Buoyancy-driven fast inertial waves generate and segregate oppositely signed helicity in spherical dynamos (Ranjan et al., 2018). That said, the intensity of slow MAC wave motions would be comparable to that of the fast waves for $|\omega_M/\omega_C| \sim 0.1$, where ω_M and ω_C are the Alfvén wave and inertial wave frequencies respectively (Sreenivasan and Maurya, 2021). Here, we examine the role of the slow MAC waves in helicity generation in the energy-containing scales of the dynamo, and hence in axial dipole formation. While earlier studies have related axisymmetric MAC waves in the stably stratified layer at the top of the core to the decadal oscillations in the Earth's field (Buffett et al., 2016), the focus of the present study is to relate non-axisymmetric MAC waves in an unstably stratified core to the formation of the dipole field. Because slow MAC waves intensify with increasing field strength, a nonlinear simulation in which the field grows from a small seed towards saturation would help us understand when the slow waves have a dominant presence alongside the fast waves in the dynamo.

Parker (1955) proposed that cyclonic motions arising from convection can generate a poloidal magnetic field from a toroidal field. Numerical dynamo simulations (Olson et al., 1999; Kageyama and Sato, 1997) lend support to this mechanism for poloidal field generation in the cores of Earth and other planets. While Takahashi and Shimizu (2012) and Penña et al. (2018) performed a detailed analysis of terms in the magnetic induction equation, the present study examines the dominant term contributions to the axial dipole field and brings out the differences between kinematic and nonlinear dynamos in this respect.

In Section 2, we describe the dynamo model and define the main dimensionless parameters used in this study. Section 3 builds on a recent study that suggested field-induced helicity generation in the relatively large scales of the dynamo (Sreenivasan and Kar, 2018) and shows through force balances that local magnetostrophy can exist in these scales where the Lorentz forces are small in the global balance. Section 4 analyses the fundamental frequencies in the dynamo and shows that the MAC wave window of azimuthal wavenumbers is indeed where the axial dipole is predominantly generated. In Section 5, the slow MAC waves in nonlinear dynamo simulations are identified by group velocity measurements. Section 6 gives the contributions to the axial dipole of the dominant terms in the induction equation in nonlinear and kinematic dynamo simulations. In conclusion, the main results of this study are summarized and its implications for polarity reversals in strongly driven dynamos are discussed.

2. Numerical dynamo model

We consider dynamo action in an electrically conducting fluid confined between two concentric, corotating spherical surfaces that correspond to the inner core boundary (ICB) and the CMB. The ratio of inner to outer radius is 0.35. Fluid motion is driven by thermal buoyancy-driven convection, although our set of equations may also be used to study thermochemical convection using the codensity formulation (Braginsky and Roberts, 1995). The other body forces acting on the fluid are the Lorentz force, arising from the interaction between the induced electric currents and the magnetic fields and the Coriolis force originating from the background rotation. The governing equations are those in the Boussinesq approximation (Kono and Roberts, 2002). Lengths are scaled by the thickness of the spherical shell L, and time is scaled by the magnetic diffusion time, L^2/η, where η is the magnetic diffusivity. The velocity field $\boldsymbol{u}$ is scaled by η/L, the magnetic field $\boldsymbol{B}$ is scaled by $(2\Omega\rho\mu\eta)^{1/2}$ where Ω is the rotation rate, ρ is the fluid density and μ is the magnetic permeability. The root mean square (rms) and peak values of the scaled magnetic field (Elsasser number Λ) are outputs derived from our dynamo simulations, where the mean is a volume average.

The non-dimensional magnetohydrodynamic (MHD) equations for the velocity, magnetic field and temperature are given by,

$$EPm^{-1}\left(\frac{\partial \mathbf{u}}{\partial t} + (\nabla \times \boldsymbol{u}) \times \boldsymbol{u}\right) + \hat{z} \times \boldsymbol{u} = -\nabla p^{\star} + Ra\,Pm Pr^{-1}\, T\boldsymbol{r} + (\nabla \times \boldsymbol{B}) \times \boldsymbol{B} + E\nabla^2 \boldsymbol{u}, \tag{1}$$

$$\frac{\partial \boldsymbol{B}}{\partial t} = \nabla \times (\boldsymbol{u} \times \boldsymbol{B}) + \nabla^2 \boldsymbol{B}, \tag{2}$$

$$\frac{\partial T}{\partial t} + (\boldsymbol{u}\cdot\nabla)T = Pm Pr^{-1}\nabla^2 T, \tag{3}$$

$$\nabla\cdot\boldsymbol{u} = \nabla\cdot\boldsymbol{B} = 0, \tag{4}$$

The modified pressure p^{*} in eq. (1) is given by $p + EPm^{-1}|\boldsymbol{u}|^2$. The dimensionless parameters in the above equations are the Ekman number $E = \nu/2\Omega L^2$, the Prandtl number, $Pr = \nu/\kappa$, the magnetic Prandtl number, $Pm = \nu/\eta$ and the modified Rayleigh number $g\alpha L\Delta T/2\Omega\kappa$. Here, g is the gravitational acceleration, ν is the kinematic viscosity, κ is the thermal diffusivity and α is the thermal expansion coefficient.

The basic-state temperature profile represents a basal heating given by $T_0(r) = \beta/r$, where β is a constant. We set isothermal conditions at both boundaries. The velocity and magnetic fields satisfy the no-slip and electrically insulating conditions, respectively. The calculations are performed by a pseudospectral code that uses spherical harmonic expansions in the angular coordinates (θ, ϕ) and finite differences in radius r (Willis et al., 2007).

For the Ekman numbers $E \sim 10^{-5}$–10^{-6} used in this study, the values of Pm chosen (Table 1) are greater than the critical values prescribed for strong-field numerical dynamos (Dormy, 2016). Furthermore, our choice of Pm ensures that the inertial forces are small relative to the Coriolis forces in the equation of motion (Sreenivasan and Jones, 2006), an essential regime for rapidly rotating planetary cores.

The convection-driven hydrodynamic dynamo is obtained by solving the equations for momentum, heat and magnetic field simultaneously, except that the Lorentz force is absent in the momentum equation. This dynamo is essentially kinematic in the sense that the back-reaction of the magnetic field on the flow is absent (see Ponty et al., 2001; Currie and Tobias, 2019).

3. Helicity generation during magnetic field growth from a seed

In line with earlier studies (Sreenivasan and Jones, 2011; Sreenivasan and Kar, 2018), we examine the evolution of the dynamo from an initial dipole-dominated seed magnetic field of intensity $\bar{B} = 0.01$. The initial velocity field is the same as that in the equivalent saturated non-magnetic run. The key output parameters of the simulations, given in Table 1, are time-averaged values in the saturated state of the dynamo. Here, the mean spherical harmonic degrees for convection and energy injection are defined by.

$$l_c = \frac{\Sigma l E_k(l)}{\Sigma E_k(l)};\ l_E = \frac{\Sigma l E_T(l)}{\Sigma E_T(l)}, \tag{5}$$

where $E_k(l)$ is the kinetic energy spectrum and $E_T(l)$ is the spectrum

Table 1
Summary of the key input and output parameters in the dynamo simulations considered in the present study. Here, N_r is the number of radial grid points, l_{max} is the maximum spherical harmonic degree, $\bar{B}$ is the volume-averaged root mean square value of the magnetic field, B_{10}^p is the poloidal axial dipole field, Ra_c is the critical Rayleigh number for the onset of nonmagnetic convection, Rm is the magnetic Reynolds number, l_c and l_E are the mean spherical harmonic degrees for convection and energy injection respectively (defined in (5)) and Ro_ℓ is the local Rossby number. The values given in brackets are those for the reference nonmagnetic runs.

S.No.	E	Ra	Ra/Ra_c	Pm	Pr	N_r	l_{max}	$\bar{B}$	B_{10}^p	Rm	l_c	l_E	Ro_ℓ
a	1.2×10^{-5}	220	4.2	5	5	120	100	0.7	0.30	105	21 (28)	20 (29)	8.42×10^{-4}
b	1.2×10^{-5}	500	9.6	5	5	144	120	1.68	0.80	184	23 (34)	23 (32)	1.61×10^{-3}
c	1.2×10^{-5}	1000	19.2	5	5	168	176	2.31	0.88	326	26 (35)	29 (37)	3.23×10^{-3}
d	1.2×10^{-5}	2000	38.5	5	5	192	224	3.05	0.96	558	28 (39)	33 (40)	5.96×10^{-3}
e	1.2×10^{-5}	5000	96.1	5	5	180	224	3.79	0.87	1218	31 (22)	42 (31)	1.44×10^{-2}
f	1.2×10^{-5}	15,000	288.4	5	5	288	280	6.21	0.84	2710	33 (21)	46 (36)	3.41×10^{-2}
g	1.2×10^{-6}	400	7.3	1	1	192	220	0.86	0.3	215	39 (43)	31 (49)	3.20×10^{-3}

obtained from the product of $u_r T$ and its conjugate. The local Rossby number Ro_ℓ, which gives the ratio of inertial to Coriolis forces on the characteristic length scale of convection (Christensen and Aubert, 2006) takes values < 0.1 (Table 1), which indicates that nonlinear inertia is not significant in our calculations.

The value of f_{dip}, which measures the relative energy contained in the axial dipole (Christensen and Aubert, 2006), shows that the field loses its dipolar character and only regains it after passing through a non-dipolar phase (Fig. 1). The snapshots of the radial magnetic field at the outer boundary during this process can be found in a previous paper (Sreenivasan and Kar, 2018) and hence not reproduced here. By visual inspection of the radial field at the outer boundary, the dipole is said to have formed when the reverse flux patches in the Northern and Southern hemispheres disappear. All runs starting from a seed magnetic field produce an approximately dipolar field for $f_{dip} > 0.7$. Dynamo saturation occurs only later than dipole formation. The time for formation of dipole decreases at high Ra. The progressive increase of the magnetic field intensity during dynamo evolution is accompanied by an increase of the axial velocity in the "large" energy-containing scales. The scales are separated by the mean harmonic degree of energy injection, l_E. There is little or no increase of the velocity in the scales $l > l_E$.

From Fig. 2, we note that the time of formation of the dipole roughly corresponds with the saturation of the axial velocity u_z in the large scales. For the moderate forcing considered here ($Ra/Ra_c \sim 10$), the extraction of kinetic energy from the small scales, due to the Lorentz force occurs only near the formation of the dipole. The magnetic field is fed by this kinetic energy but the growth of magnetic energy is not much due to this process. The extraction of energy occurs in a relatively short time. Thus, the growth of energy in the large scales and extraction of energy from the small scales remains fairly independent. We hypothesize that a quasi-linear wave excitation in the large scales of the dynamo would cause the enhancement of convective velocity over that in the equivalent nonmagnetic state. As the forcing is increased, the extraction of energy from the small scales happens before the formation of the dipole. This would mean that at higher Ra/Ra_c, the growth of magnetic field is partially fed by the kinetic energy from the small scales.

The kinetic helicity $\boldsymbol{u}\cdot\boldsymbol{\zeta}$, where $\boldsymbol{\zeta}$ is the vorticity, is considered to be an important quantity for dynamo action (e.g. Moffatt, 1978). Fig. 3 (a) and (b) show the enhancement of kinetic helicity in the large scales for the two dynamo simulations considered in Fig. 2. In cylindrical coordinates (s, ϕ, z), the magnetic field enhances the axial (z) and radial (s) parts of the helicity in equal measure (Sreenivasan and Jones, 2011). Therefore, the sum of the z and s parts of the helicity is considered. A notable finding is that the dipole forms from a chaotic multipolar state when the helicity in the large scales increases by a magnitude nearly equal to the initial helicity in these scales, associated with convection in the equivalent nonmagnetic system. In the run at $E = 1.2\times10^{-6}$ and $Ra = 400$, the kinetic energy computed from the s and z velocities is found to increase by 90% of its initial value while the enstrophy (integral of the square of the vorticity) increases by 30%. Table 2 shows the sum of peak z and s helicity attained during the growth of the magnetic field for the lower half of the shell. For moderate Ra, the total helicity over all scales during the growth of the magnetic field is higher than the nonmagnetic value as extraction of kinetic energy from the small scales occurs only near the dipole formation time. This is illustrated in Fig. 3 (c), where at $t_d = 0.26$, peak helicity growth occurs such that the helicity in the dynamo exceeds the nonmagnetic helicity for all scales. By time $t_d = 0.28$ (Fig. 3 (d)), energy extraction would begin and the helicity in the small scales would fall below the nonmagnetic values. By the time the dynamo reaches saturation, the helicity in the small scales would have fallen even further. The helicity deficit in the small scales dominates the helicity generated in the large scales and therefore the total helicity in the saturated dynamo is always less than its nonmagnetic counterpart. For higher Ra, the total helicity would always be less than that in the nonmagnetic case as the energy extraction from the small scales occurs much before dipole formation. The helicity in the large scales would,

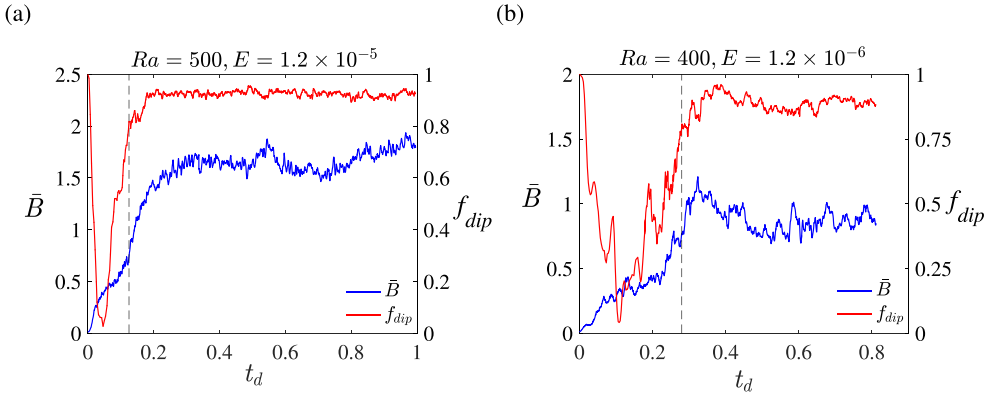

Fig. 1. Evolution in time (measured in units of magnetic diffusion time) of the magnetic field intensity given by its volume averaged root mean square value, $\bar{B}$ and f_{dip} (a measure of the axial dipole strength). The axial dipole formation time, marked by the vertical dashed line, is at $t_d = 0.125$ in (a) and $t_d = 0.28$ in (b).

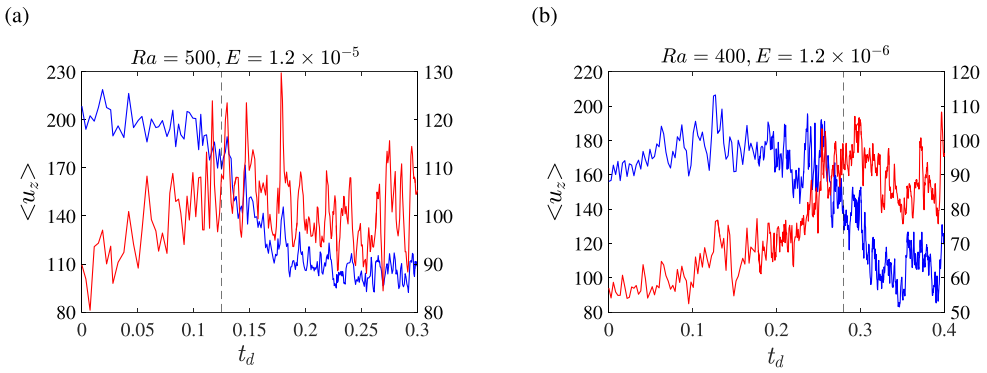

Fig. 2. Root mean square value of the axial velocity u_z for two ranges of spherical harmonic degree, l. The scales considered are $l \leq 23$ (red) in (a) and $l \leq 31$ (red) in (b), $l > 23$ (blue) in (a) and $l > 31$ (blue) in (b). The mean harmonic degree of energy injection l_E serves as the basis for separation of scales. The vertical dashed lines indicate the dipole formation times. (For interpretation of the references to colour in this figure legend, the reader is referred to the web version of this article.)

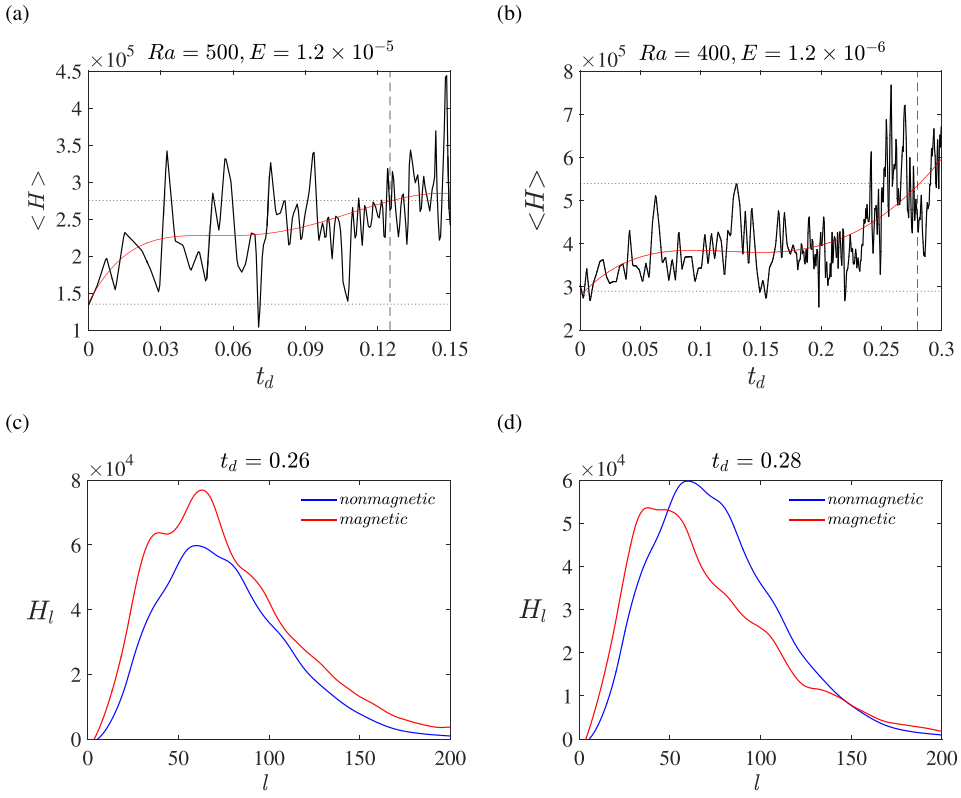

Fig. 3. (a) & (b) Sum of the axial (z) and radial (s) helicity $< H >$ for the lower half of the spherical shell, plotted against time (measured in units of the magnetic diffusion time t_d). The scales considered are $l \leq 23$ for (a) and $l \leq 31$ for (b). The dynamo parameters are $Ra = 500$, $Pm = Pr = 5$, $E = 1.2 \times 10^{-5}$ for (a) and $Ra = 400$, $Pm = Pr = 1$, $E = 1.2 \times 10^{-6}$ for (b). The dashed vertical line indicates dipole formation time. (c) & (d) Distribution of helicity over spherical harmonic degree at two times near dipole formation for the simulation in (b).

however, still exceed the helicity of the nonmagnetic case.

Ranjan et al. (2020) show that the helicity source term due to the Lorentz force is negatively correlated with the overall helicity distribution. They attributed the distribution of helicity in the core to inertial waves. No scale separation was performed, so the overall helicity for the saturated dynamo was lower than that for the nonmagnetic state. Their result is consistent with our analysis considering all scales (Table 2). To show that the slow MAC waves might cause the increase of dynamo helicity over the nonmagnetic value at scales $l \leq l_E$, one must first look at the scale-separated force balance in the dynamo.

3.1. Scale-dependent balance of forces

Dipole-dominated dynamos are known to exist in the so-called MAC regime where Lorentz, buoyancy and Coriolis forces are dominant (Sreenivasan and Jones, 2006) and the nonlinear inertial and viscous forces are negligible. The Lorentz forces may, however, be localized due to spatially inhomogeneous magnetic flux. In line with earlier studies (Sreenivasan and Jones, 2006), we examine the ratio of the Lorentz, Coriolis and buoyancy forces in the z vorticity equation to the highest force among them for two distinct ranges of the spherical harmonic degree.

In the dynamo simulation at $E = 1.2 \times 10^{-6}$ and $Ra = 400$, the Coriolis and buoyancy forces are in approximate balance for the relatively large scales $l \leq 31$ (Fig. 4 (b) and (c)). However, as seen in Fig. 4(a), the Lorentz forces become significant in patches and balance the Coriolis forces. Therefore, localized excitation of slow MAC waves in these scales is anticipated. For the small scales of $l > 100$, the buoyancy forces are restricted to the outer periphery of the shell (Fig. 4 (e)). The dominant balance in these scales is between the Lorentz and Coriolis forces (Fig. 4

Table 2
Sum of the axial (z) and and radial (s) parts of the kinetic helicity for the large (energy-containing) scales and for all scales evaluated at two times during the evolution of the dynamo magnetic field from a seed state. The helicity is evaluated for the lower half of the spherical shell. The nonmagnetic helicity is given in brackets. The large scales are those for $l \leq l_E$, where l_E is the mean harmonic degree of energy injection in the dynamo.

S.No.	E, Ra	time (t_d)	Scales	Helicity
(i)	1.2×10^{-5}, 500	0.095	$l \leq 23$	3.21×10^{5} (1.34×10^{5})
			All	7.66×10^{6} (7.23×10^{6})
		0.125	$l \leq 23$	2.81×10^{5} (1.34×10^{5})
			All	6.41×10^{6} (7.23×10^{6})
(ii)	1.2×10^{-6}, 400	0.26	$l \leq 31$	6.89×10^{5} (3.05×10^{5})
			All	7.15×10^{6} (4.85×10^{6})
		0.28	$l \leq 31$	6.72×10^{5} (3.05×10^{5})
			All	3.89×10^{6} (4.85×10^{6})

(d) and 4 (f)). In either range of harmonic degrees, the nonlinear inertial and viscous forces are small compared with the other forces in the bulk of the volume, and hence not shown.

Before discussing the role of the slow MAC waves in the dynamo, we examine the relative magnitudes of the fundamental frequencies and show that wave motions correlate with helicity generation and dipole formation in the energy-containing scales.

4. MAC waves, helicity and dipole formation

Forced MHD waves in planetary cores are produced by isolated density disturbances that evolve subject to background rotation and a mean magnetic field. For simplicity, we relate a density perturbation ρ' to the temperature perturbation T' by $\rho' = -\rho\alpha T'$, where ρ is the ambient density and α is the coefficient of thermal expansion. The velocity perturbation $\boldsymbol{u}'$ produced by T' interacts with the mean magnetic field to generate the induced field $\boldsymbol{b}'$. For zero mean flow, the linearized equations for $\boldsymbol{u}'$, $\boldsymbol{b}'$ and T' are solved by seeking plane wave solutions for the perturbation variables. In the diffusionless limit ($\nu = \kappa = \eta = 0$), the following characteristic equation is obtained for the frequencies of the system (Busse et al., 2007; Sreenivasan and Maurya, 2021):

$$\left(\omega^2 - \omega_M^2 - \omega_A^2\right)\left(\omega^2 - \omega_M^2\right) - \omega_C^2\omega^2 = 0, \tag{6}$$

where the fundamental frequencies ω_M, ω_A and ω_C represent Alfvén waves, internal gravity waves and linear inertial waves respectively. In unstable stratification that drives planetary core convection, $\omega_A^2 < 0$, where $|\omega_A|$ is simply a measure of the strength of buoyancy. Although the magnetic field in the dynamo is time varying, wave motions can be analyzed in small time intervals where the ambient field is approximately steady.

The dimensional frequencies ω_M^2, $-\omega_A^2$ and ω_C^2 in the dynamo are given by

$$\omega_M^2 = \frac{(\boldsymbol{B}\cdot\boldsymbol{k})^2}{\mu\rho}, \quad -\omega_A^2 = g\alpha\beta\left(\frac{k_z^2+k_\phi^2}{k^2}\right), \quad \omega_C^2 = \frac{4(\boldsymbol{\Omega}\cdot\boldsymbol{k})^2}{k^2},$$

and scaling the frequencies by η/L^2, we obtain in dimensionless units,

$$\omega_M^2 = \frac{Pm}{E}(\boldsymbol{B}\cdot\boldsymbol{k})^2, \quad -\omega_A^2 = \frac{Pm^2Ra}{PrE}\left(\frac{k_z^2+k_\phi^2}{k^2}\right), \quad \omega_C^2 = \frac{Pm^2}{E^2}\frac{k_z^2}{k^2}, \tag{7}$$

where k_s, k_ϕ and k_z are the radial, azimuthal and axial wavenumbers in cylindrical coordinates (s,ϕ,z), $k_\phi = m/s$, where m is the spherical harmonic order, and $k^2 = k_s^2 + k_\phi^2 + k_z^2$. Here, ω_A is evaluated on the equatorial plane where the buoyancy force is maximum; ω_M is based on the measured peak magnetic field in the dynamo. The wavenumber k_ϕ is evaluated at $s = 1$, approximately mid-radius of the spherical shell.

For the inequality $|\omega_C| > |\omega_M| > |\omega_A|$, the roots of eq. (6),

$$\omega_f = \pm\frac{1}{\sqrt{2}}\sqrt{\omega_A^2 + \omega_C^2 + 2\omega_M^2 + \sqrt{\omega_A^4 + 2\omega_A^2\omega_C^2 + 4\omega_M^2\omega_C^2 + \omega_C^4}}, \tag{8}$$

$$\omega_s = \pm\frac{1}{\sqrt{2}}\sqrt{\omega_A^2 + \omega_C^2 + 2\omega_M^2 - \sqrt{\omega_A^4 + 2\omega_A^2\omega_C^2 + 4\omega_M^2\omega_C^2 + \omega_C^4}}. \tag{9}$$

represent the fast (f) and slow (s) MAC waves. While the fast waves are linear inertial waves weakly modified by the magnetic field and buoyancy, the slow waves are magnetostrophic (Braginsky, 1967; Acheson and Hide, 1973; Busse et al., 2007).

In fig. 5(a) and (b), the magnitudes of the fundamental frequencies are shown as a function of the azimuthal wavenumber m. Two times are analyzed in the growth phase of the dynamo run at $E = 1.2\times10^{-6}$, $Ra = 400$ and $Pr = Pm = 1$. The frequencies are computed from (7) using the mean values of the s and z wavenumbers. For example, real space integration over (s,ϕ) gives the kinetic energy as a function of z, the Fourier transform of which gives the one-dimensional spectrum $\hat{u}^2(k_z)$. Subsequently, we obtain

$$\bar{k}_z = \frac{\Sigma k_z\,\hat{u}^2(k_z)}{\Sigma\hat{u}^2(k_z)}. \tag{10}$$

A similar approach gives $\bar{k}_s$. The computed frequencies in fig. 5(a) and (b) satisfy the inequality $|\omega_C| > |\omega_M| > |\omega_A|$ in the energy-containing scales of the dynamo spectrum, indicating that the MAC waves would be generated in these scales. We emphasize that this inequality would be obtained only if the measured peak magnetic field is used in the evaluation of ω_M, corresponding to local Elsasser numbers $\Lambda \gg 1$ (see Sreenivasan and Maurya (2021) and Fig. 14 in Section 7). The range of scales with the above frequency inequality narrows as the field intensity increases in time, and close to dipole formation ($t_d = 0.275$), this inequality is confined to wavenumbers $m < 19$. The wavenumbers of helicity generation (shown in shaded grey bands) are obtained from the differences between the helicity spectra of the dynamo and equivalent nonmagnetic runs, and show the scales where the dynamo helicity is greater than the nonmagnetic helicity. Notably, the region of helicity generation overlaps with the scales where the MAC waves are generated. The slow MAC wave frequency merges with the Alfvén wave frequency at large m, where ω_M is the dominant frequency.

The power supplied by convection to the poloidal axial dipole field $\boldsymbol{B}_{10}^P$ is given by (e.g. Buffett and Bloxham, 2002)

$$\Gamma_{10}^P = \int_V \boldsymbol{B}_{10}^P\cdot[\nabla\times(\boldsymbol{u}\times\boldsymbol{B})]dV. \tag{11}$$

The spectral distribution of Γ_{10}^P, given by

$$P_{10} = \int_V \boldsymbol{B}_{10}^P\cdot\left[\nabla\times(\boldsymbol{u}\times\boldsymbol{B})_m\right]dV,$$

is the power supplied to the dipole field from individual spherical harmonic order (m) components of $\nabla\times(\boldsymbol{u}\times\boldsymbol{B})$. From Fig. 5 (c) and (d), it is evident that the largest contribution to the dipole field occurs in the scales where helicity is generated by the magnetic field. The strong correlation between MAC wave formation, helicity generation, and in turn, the axial dipole field energy, is also noted in the dynamo simulations at $E = 1.2\times10^{-5}$.

Fig. 6(a) and (b) shows the fundamental frequencies and the slow MAC wave frequency plotted against time for two dynamo simulations that begin from a small seed magnetic field. The frequencies are calculated at a wavenumber $\bar{m}$, obtained through a weighted average as in (10), but over the range of m where the inequality $|\omega_C| > |\omega_M| > |\omega_A|$ holds at dipole formation time. The dimensionless magnetic diffusion frequency is given by $\omega_\eta = \bar{k}^2L^2$, where $\bar{k}^2 = \bar{k}_s^2 + \bar{k}_\phi^2 + \bar{k}_z^2$.

Approximation of the right-hand side of (9) by retaining terms up to

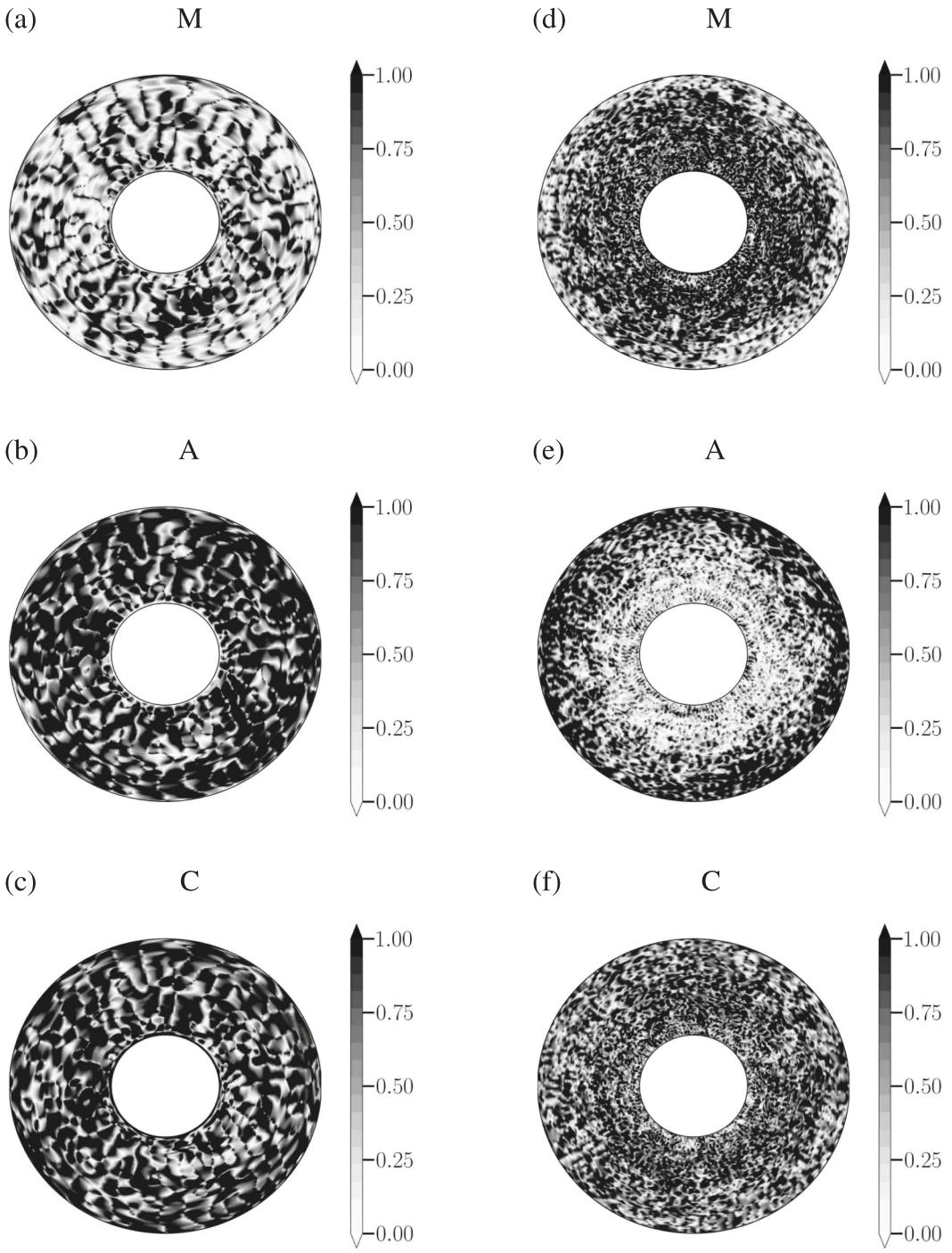

Fig. 4. The ratio of magnitudes of the magnetic Lorentz (M), buoyancy (A) and Coriolis (C) force terms in the z-vorticity equation to the magnitude of the largest force among them, is plotted on the horizontal section $z = 0.1$ for two ranges of scales $l \leq 31$ in ((a)-(c)) and $l > 100$ in ((d)-(f)). The model parameters are $Ra = 400$, $Pm = Pr = 1$, $E = 1.2 \times 10^{-6}$.

second order in ω_M/ω_C and ω_A/ω_C gives (Braginsky, 1967; Busse et al., 2007)

$$\omega_s \approx \frac{\omega_M^2}{\omega_C}\left(1 + \frac{\omega_A^2}{\omega_M^2}\right)^{1/2}, \tag{12}$$

where ω_M^2/ω_C is the Magneto-Coriolis (MC) wave frequency. In an unstably stratified fluid, slow MAC waves would be generated only for $|\omega_M| > |\omega_A|$, the boundary of which is marked by the dashed vertical lines in Fig. 6. Notably, the increase in f_{dip}, which measures the relative axial dipole strength (Fig. 1), occurs at times after the onset of slow MAC waves (Fig. 6).

The Lehnert number in the dynamo simulations, evaluated by

$$Le = |\boldsymbol{B}|\left(\frac{E}{Pm}\right)^{1/2}\frac{m}{2\pi}, \tag{13}$$

has its origin in $(\omega_M/\omega_C)_0$, the frequency ratio at the initial state of a buoyant blob released into the flow (Sreenivasan and Maurya, 2021). As blobs evolve in time into columns, the wavenumber k_z decreases relative to m, so the instantaneous value of (ω_M/ω_C) is at least one order of magnitude higher than Le (Table 3). For values of $(\omega_M/\omega_C) \sim 0.1$, the

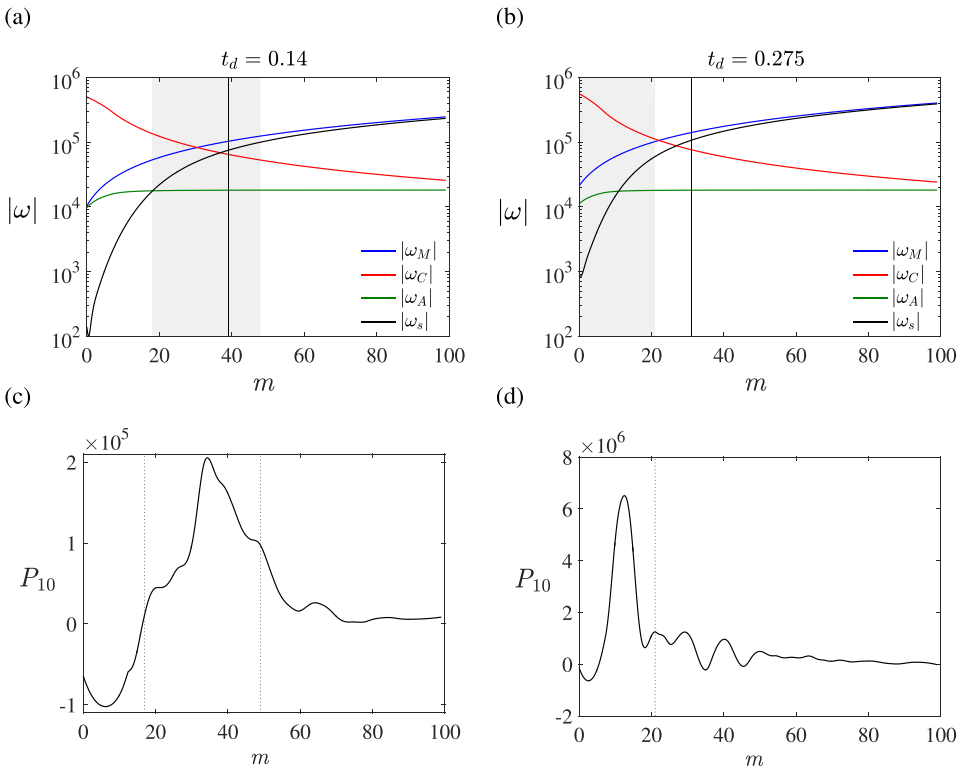

Fig. 5. (a) & (b): Absolute values of frequencies plotted for two snapshots of time during the evolution of the dynamo from a small seed field magnetic field. The magnitudes of the following frequencies are shown: ω_C (linear inertial wave), ω_M (Alfvén wave), ω_A (internal gravity wave) and ω_s (slow MAC wave). Since $\omega_A^2 < 0$ in unstable stratification, ω_A is simply a measure of the strength of buoyancy in the dynamo. The shaded grey area shows the scales where helicity is generated in the dynamo simulation relative to the nonmagnetic simulation. The thin solid vertical line shows the mean wave number of energy injection. (c) & (d): Spectral distribution of the power supplied to the axial dipole, given by $P_{10} = \int_V \boldsymbol{B}_{10}^P \cdot [\nabla \times (\boldsymbol{u} \times \boldsymbol{B})_m] \, dV$. The vertical dotted lines show the same range of scales as in (a) & (b), where helicity is generated. The dynamo parameters are $Ra = 400$, $Pm = Pr = 1$, $E = 1.2 \times 10^{-6}$.

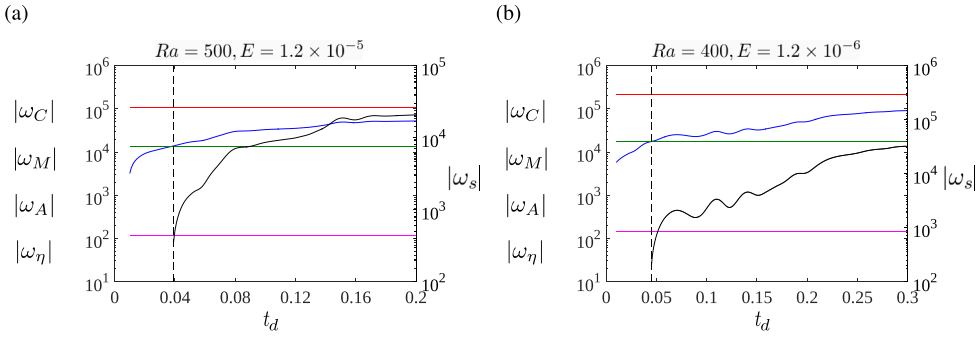

Fig. 6. Absolute values of the dynamo frequencies plotted against time (in units of the magnetic diffusion time t_d). Both the simulations study the evolution of the dynamo starting from a small seed magnetic field. The frequencies are calculated at the mean azimuthal wavenumber ($\bar{m} = 10$ for (a) and 11 for (b)) of the range of scales where MAC waves are active at dipole formation time. The axial dipole forms from a multipolar state at $t_d \approx 0.125$ in (a) and $t_d \approx 0.28$ in (b). The dashed vertical lines indicate the times at which the slow MAC waves are first generated. The frequencies shown (with line colours in brackets) are as follows: ω_M (blue), ω_C (red), ω_A (green), ω_η (magenta), ω_s (black). (For interpretation of the references to colour in this figure legend, the reader is referred to the web version of this article.)

Table 3
Comparison of the values of the Lehnert number Le and the frequency ratio ω_M/ω_C at three points in time (in units of the magnetic diffusion time t_d) during the growth phase of two dynamo models. The times considered are those at incipient slow MAC wave generation, onset of helicity generation, and axial dipole formation. The evolution in time of the measured frequencies in these models is shown in Fig. 6(a) and (b).

$E = 1.2 \times 10^{-5}$, $Ra = 500$			$E = 1.2 \times 10^{-6}$, $Ra = 400$		
t_d	ω_M/ω_C	Le	t_d	ω_M/ω_C	Le
0.033	0.108	0.005	0.041	0.076	0.003
0.04	0.147	0.006	0.14	0.162	0.0065
0.125	0.310	0.014	0.28	0.345	0.014

intensity of slow MAC wave motions would be comparable to that of the fast waves (Sreenivasan and Maurya, 2021). Consequently, one would expect the helicity generated by the slow wave motions to be of the same order of magnitude as that of the fast waves. The approximately two-fold increase in the helicity as the dynamo evolves from a seed magnetic field (fig. 3 (a) & (b)) suggests that the helicity generated by slow wave motions in the dynamo may be comparable to that produced by the fast inertial waves in nonmagnetic convection.

While the frequency diagrams in Fig. 5 and Fig. 6 suggest the active role of slow MAC waves in dipole formation, conclusive evidence for the existence of these waves necessitates visualization of their propagation, which is presented in the following section.

5. Identification of slow MAC waves in the dynamo

Isolated blobs of buoyant fluid evolve into columnar vortices aligned with the axis of rotation through the propagation of damped fast and

slow MAC waves. This process is best understood by studying axial motions in rapidly rotating dynamos for several small windows of time spanning the evolution of magnetic field. The ambient magnetic field and the wavenumbers are approximately constant in these time windows. Analysis of simulations in which the magnetic field increases from a small seed value gives a good insight into the conditions for the formation and eventual dominance of slow MAC waves. Following from Section 3, where the generation of field-induced helicity was found to occur in the energy-containing scales $l \leq l_E$, the measurement of axial motions is limited to these scales.

Two videos given in Supplementary Information show the propagation of isolated blobs situated in the axial flow (u_z) field in a dynamo simulation starting from a small seed magnetic field. The parameters $E = 1.2 \times 10^{-6}$, $Ra = 400$, and $Pr = Pm = 1$ are used. In a small time window in the neighbourhood of $t_d \approx 0.23$, the axial location of blob fronts (z_f) is measured at cylindrical radius $s = 1$. The average velocities of propagation obtained from the two videos (2853 and 2308 respectively) are compared with the axial group velocity of waves generated in the time window. This velocity is estimated for the fast (f) and slow (s) MAC waves by taking the derivatives of the respective frequencies given in (8) and (9) with respect to the z wavenumber (Vallis, 2006, pp. 238–239),

$$U_f = \frac{\partial \omega_f}{\partial k_z}; \quad U_s = \frac{\partial \omega_s}{\partial k_z}. \tag{14}$$

The frequencies above are calculated using all three components of the magnetic field at the peak-field location, mean wavenumbers $\bar{k}_s$ and $\bar{k}_z$ in the range $l \leq l_E$, and the mean wavenumber $\bar{m}$ over the m-range where the inequality $|\omega_C| > |\omega_M| > |\omega_A|$ holds (within $l \leq l_E$). In the neighbourhood of time $t_d \approx 0.23$, $U_f \approx 38000$ and $U_s \approx 2700$; it is therefore evident that the blob fronts propagate at a speed comparable to the group velocity of the slow MAC waves. While recent studies (Hori et al., 2015; Chi-Durn et al., 2020) have measured propagation velocities for a selected wavenumber m, here we measure the velocity of structures within $l \leq l_E$ with no restriction on the wavenumber, which gives a meaningful comparison with the group velocity.

Fig. 7 shows the measurement of wave motion in the dynamo simulation with $E = 1.2 \times 10^{-6}$ and $Ra = 400$ at different time windows during the growth of the field from a small seed value. Wave motion is analyzed through contour plots of $\dot{u}_z$ at points on the cylindrical radius $s = 1$. These contours show the propagation paths of the fluctuating z velocity; the contours of u_z would be nearly similar due to the small mean z velocity. The range $l \leq l_E$ narrows down with increasing field intensity. At early times ($t_d = 0.0375$–0.039), when the field intensity is so small that $|\omega_M| < |\omega_A|$, only fast MAC waves are present (Fig. 7(a) and Table 4). As the field intensity increases with time in the dynamo, the group velocity measurements confirm the presence of slow MAC waves in the large scales. Slow wave parcels originating from points far from the equatorial plane ($z = 0$) are seen to propagate in opposite directions with nearly equal velocity (e.g. Fig. 7(b)). While the slow waves co-exist with the fast waves (not at the same location) at times $t_d = 0.231$–0.233 (Fig. 7(c)), the slow waves are dominant close to dipole formation ($t_d = 0.271$–0.276; Fig. 7(d)). The measured group velocity $U_{g,z}$ increases with field intensity (Table 4), which is the hallmark of the slow waves whose frequency ω_s increases with increasing ω_M. Because U_f is at least one order of magnitude higher than U_s, the fair agreement between $U_{g,z}$ and U_s cannot be missed. The dominance of the fast waves for weak fields and the slow waves for strong fields is further evident in Fig. 8, where the fast Fourier transform (FFT) of $\dot{u}_z$ is shown. In line with the group velocity measurements, the flow is made up of waves of frequency $\omega \sim \omega_f$ for weak fields (Fig. 8(a)), whereas for the stronger fields close to dipole formation ((Fig. 8(b)), waves of much lower frequency $\omega \sim \omega_s$ are dominant.

The contour plots of the time variation of the magnetic field $\dot{B}_z$ indicate that slow MAC wave motions are dominant even at early times

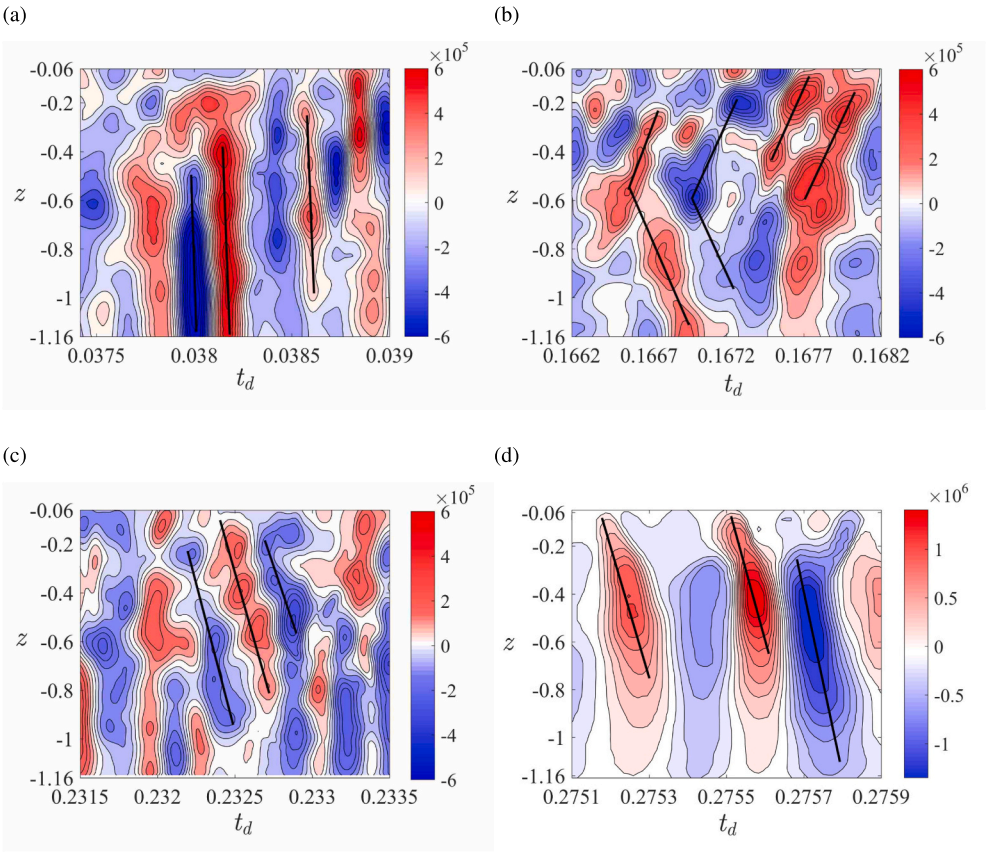

Fig. 7. (a) Contour plot of $\dot{u}_z$ at cylindrical radius $s = 1$ for the time interval $t_d = 0.0375$–0.039 and $l \leq 42$. (b) $\dot{u}_z$ for the time interval $t_d = 0.166$–0.168 and $l \leq 40$. (c) $\dot{u}_z$ for the time interval $t_d = 0.231$–0.234 and $l \leq 36$. (c) $\dot{u}_z$ for the time interval $t_d = 0.275$–0.276 and $l \leq 31$. The parameters of the dynamo simulation are $E = 1.2 \times 10^{-6}$, $Ra = 400$, $Pm = Pr = 1$. The nearly parallel black lines indicate the predominant direction of travel of the waves and their slope gives the group velocity. The estimated group velocity of the fast and slow MAC waves (U_f and U_s respectively) and the measured group velocity $U_{g,z}$ are given in Table 4.

Table 4
Summary of the data for MAC wave identification in the dynamo simulations. Scales given by $l \leq l_E$, where l_E is the mean harmonic degree of energy injection, are considered in each case. The sampling frequency ω_n is chosen to ensure that the fast MAC waves are not missed in the measurement of group velocity. The values of ω_M^2, $-\omega_A^2$ and ω_C^2 are calculated from (7) using the mean wavenumbers $\bar{m}$, $\bar{k}_s$ and $\bar{k}_z$. The measured group velocity in the z direction ($U_{g.z}$) may be compared with the estimated fast (U_f) or slow (U_s) MAC wave velocity, as appropriate. *Case (ix) is a kinematic dynamo simulation, which does not produce an axial dipole.

S.No.	E	Ra	Fig. no.	$\omega_n(\times 10^5)$	Scales	$\bar{m}$	$\bar{k}_s$	$\bar{k}_z$	$\omega_M^2(\times 10^9)$	$-\omega_A^2(\times 10^9)$	$\omega_C^2(\times 10^9)$	U_s	U_f	$U_{g.z}$
(i)	1.2×10^{-6}	400	7(a)	6.67	$l\leq 42$	24	3.32	2.91	0.17	0.33	9.87	–	33820	28333
(ii)			7(b)	6.67	$l\leq 40$	23	3.15	2.14	0.49	0.33	5.85	1089	34036	1350
(iii)			7(c)	5	$l\leq 36$	20	3.02	2.19	0.77	0.32	8.04	1982	38374	2667
(iv)			7(d)	5	$l\leq 31$	10	3.05	2.11	3.66	0.31	27.1	5295	69765	6534
(v)			9(a)	6.67	$l\leq 42$	11	3.61	1.43	3.9	0.30	10.4	780	69137	966
(vi)			9(b)	5	$l\leq 31$	9	3.45	1.67	1.68	0.29	23.4	3625	78988	3750
(vii)	1.2×10^{-5}	2000	10(a)	3.33	$l\leq 40$	12	4.24	2.34	4.25	0.74	5.7	5071	25957	6100
(viii)	1.2×10^{-5}	15000	10(b)	1.67	$l\leq 46$	4	4.78	2.63	12.9	0.36	31.2	4856	43656	5187
(ix)*	1.2×10^{-6}	400	11	10	$l\leq 42$	16	4.95	2.64	–	–	1.68	–	48396	55000

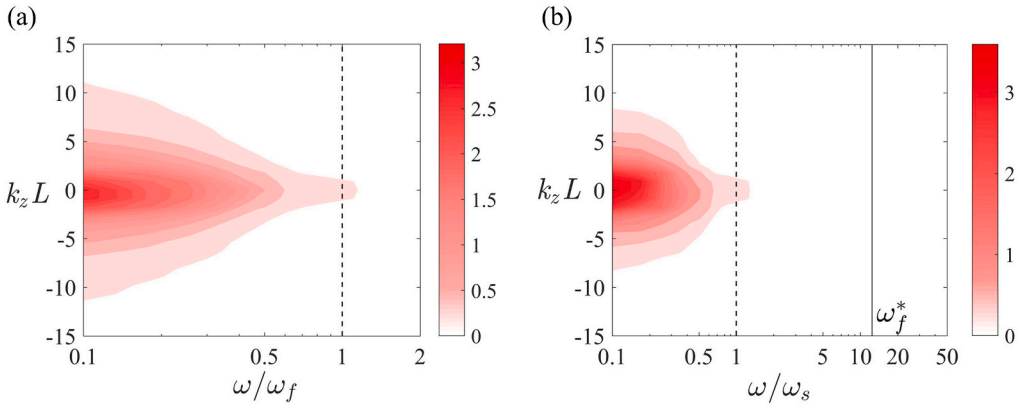

Fig. 8. (a) FFT spectrum of $\dot{u}_z$ at cylindrical radius $s = 1$ for the scales $l \leq 42$ in the time interval $t_d = 0.08 - 0.082$. (b) FFT spectrum of $\dot{u}_z$ at $s = 1$ for $l \leq 31$ in the time interval $t_d = 0.274 - 0.278$. The spectra are computed at discrete ϕ points and then averaged azimuthally. The range $l \leq l_E$ narrows down as the field intensity increases with time. The dynamo parameters are $Ra = 400$, $Pm = Pr = 1$, $E = 1.2\times10^{-6}$. The vertical dashed lines correspond to $\omega/\omega_f = 1$ in (a) and $\omega/\omega_s = 1$ in (b), where ω_f and ω_s are the estimated fast and slow MAC wave frequencies. In (b), $\omega_f^* = \omega_f/\omega_s$.

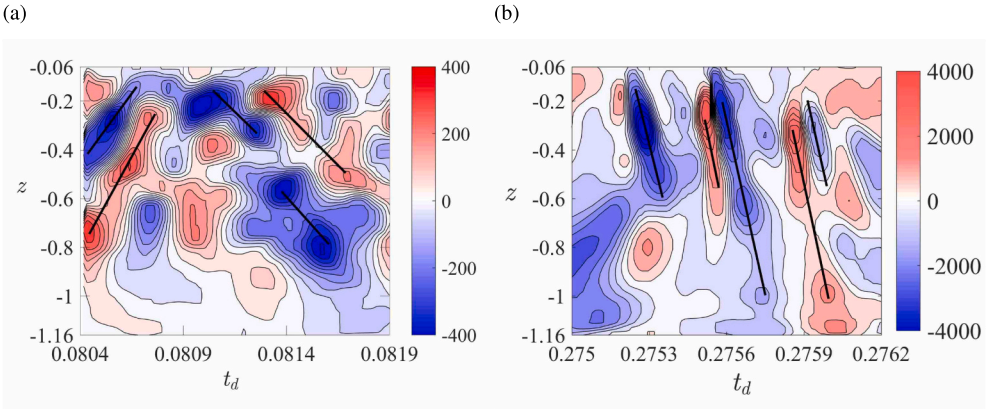

Fig. 9. Contour plots of $\dot{B}_z$ at cylindrical radius $s = 1$ shown for two time intervals. (a) $t_d = 0.063 - 0.068$, $l \leq 42$. (b) $t_d = 0.274 - 0.278$, $l \leq 31$. The nearly parallel black lines indicate the predominant direction of travel of the waves and their slope gives the measured group velocity. The dynamo parameters are $Ra = 400$, $Pm = Pr = 1$, $E = 1.2\times10^{-6}$. The estimated group velocity of the fast and slow MAC waves (U_f and U_s respectively) and the measured group velocity $U_{g.z}$ are given in Table 4.

when the field is weak (Fig. 9(a)). The measured group velocity $U_{g.z}$ is in fair agreement with the estimated slow wave velocity U_s while the fast wave velocity U_f is $O(10^2)$ higher (Table 4). (Here, the mean wavenumbers used for the theoretical estimate are those of the magnetic field.) This interesting distinction between the wave motions of the flow and field is well explained by Sreenivasan and Maurya (2021), who found that the induced magnetic field preferentially propagates as slow MAC waves for a wide range of $\omega_M/\omega_C \ll 1$ to ~ 1.

The signature of the slow waves in the energy-containing scales is also visible in strongly driven dipolar dynamos (Fig. 10). As the intensity of the self-generated field increases with increased forcing, the range of azimuthal wavenumbers m over which $|\omega_C| > |\omega_M|$ narrows down considerably (Table 4). Consequently, the generation of helicity due to the slow MAC waves is weakened, which can explain why the axial dipole field B_{10}^P diminishes in strength with increased forcing (for $Ra/Ra_c > 40$ in Table 1). The decrease in dipole field intensity is likely not due to the growth of inertial forces, for the local Rossby number Ro_ℓ is small even in the strongly driven dynamo runs. There is, however, a growing dominance of fast waves in the large scales, which does not contribute to dipole field generation. At lower Ekman number E, one would expect the MAC wave window to widen as $|\omega_C|$ increases relative to $|\omega_M|$. The choice of $Pm \gtrsim 1$ ensures a low-inertia regime conducive to MAC waves in the simulations at $E \sim 10^{-5}$–10^{-6}. From our results, we anticipate that the low-E, low-Pm regime of planetary cores would support the axial dipole through slow MAC waves in strongly driven convection. Finally, we note that only linear inertial waves are produced in kinematic dynamo simulations which produce multipolar fields (Fig. 11 and case (ix) in Table 4).

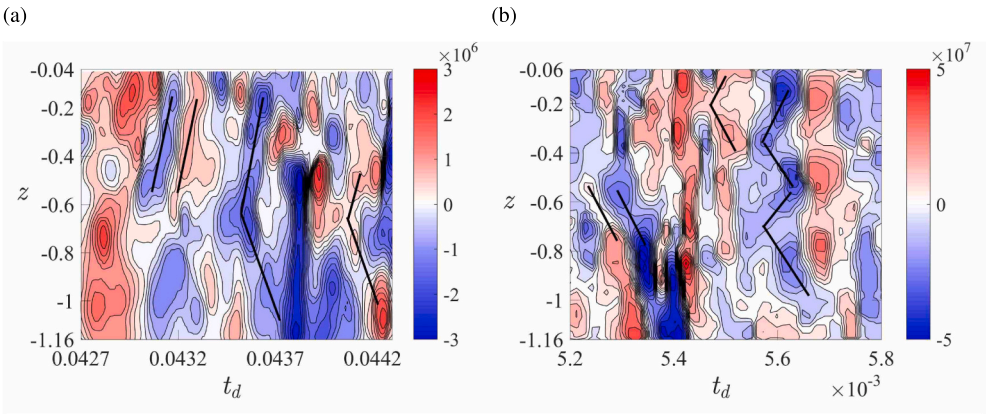

Fig. 10. (a) Contour plot of $\dot{u}_z$ at cylindrical radius $s = 1$ for $l \leq 40$ and the parameters $E = 1.2 \times 10^{-5}$, $Ra = 2000$, $Pr = Pm = 5$. (b) $\dot{u}_z$ for $l \leq 46$ and the parameters $E = 1.2 \times 10^{-5}$, $Ra = 15000$, $Pr = Pm = 5$. The nearly parallel black lines indicate the direction of travel of the waves and their slope gives the measured group velocity. The estimated group velocity of the fast and slow MAC waves (U_f and U_s respectively) and the measured group velocity $U_{g.z}$ are given in Table 4.

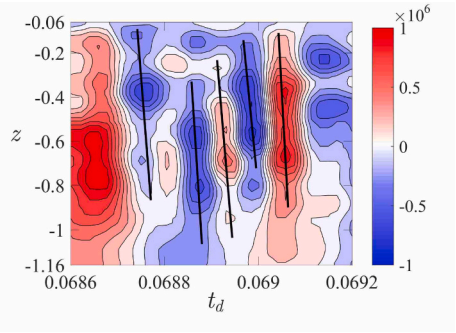

Fig. 11. Contour plot of $\dot{u}_z$ at cylindrical radius $s = 1$ for the scales $l \leq 42$ in a kinematic dynamo simulation with the parameters $E = 1.2 \times 10^{-6}$, $Ra = 400$, $Pm = Pr = 1$. The nearly parallel black lines indicate the direction of travel of the waves and their slope gives the measured group velocity. Similar plots are obtained for any time window in the simulation. The estimated group velocity of the fast and slow MAC waves (U_f and U_s respectively) and the measured group velocity $U_{g.z}$ are given in Table 4.

Buoyancy-induced inertial waves have been found in dynamo simulations though group velocity measurements (Ranjan et al., 2018). The present study has shown that slow MAC wave motions are measurable only when large scales of $l \leq l_E$ are considered. Within this range, the slow waves are predominantly generated in the MAC wave window, where $|\omega_C| > |\omega_M| > |\omega_A|$. To identify the scales where fast and slow MAC waves are active and distinguishable from each other, a scale-dependent analysis of the dynamo spectrum is essential.

5.1. Non-axisymmetric Alfvén waves

The generation of MAC waves in the dynamo is accompanied by non-axisymmetric waves along the cylindrical radius whose group velocity matches with that of Alfvén waves. The frequencies of waves that propagate orthogonal to the axis of rotation – obtained by letting $\omega_C = 0$ in eqs. (8) and (9) – would be Alfvénic for strong-field dynamos where $|\omega_C| > |\omega_M| > |\omega_A|$. In the dynamo simulation at $E = 1.2 \times 10^{-6}$ and $Ra = 400$, coherent radial motion with estimated Alfvén velocities is only noted after diffusion time $t_d \approx 0.1$. Since slow MAC waves are first excited at $t_d \approx 0.04$ during the growth phase of the dynamo (Fig. 6(b)), it is reasonable to suppose that the Alfvén waves exist as the degenerate form of the MAC waves. In the contour plots of $\dot{u}_z$ given in fig. 12 (a) and (b), the wave velocity is the slope measured over small time windows. Fig. 12 (c) shows the variation of the wave velocity with cylindrical radius s for the two time intervals in (a) and (b), with the earlier interval showing lower velocity. The peak wave velocities measured throughout the simulation show a fair agreement with the Alfvén velocities calculated from the peak value of B_s. The increase in the measured wave velocity with the increasing intensity of B_s in time is evident in fig. 12 (d). The waves slow down at the outer boundaries where the field intensity is weak. As we see below, the non-axisymmetric waves explain the growth of u_z in the s direction, an essential process in dipole formation from a seed magnetic field.

6. Termwise contributions to the axial dipole

To understand how wave motion influences the formation of the axial dipole field through the magnetic induction equation, we look at stretching and advection terms in this equation which influence the dipole. In cylindrical polar coordinates, the relative contributions of the s and z components of the terms to the dipole are given by

$$\frac{\int_V \left[\widehat{\boldsymbol{e}}_s \cdot \boldsymbol{B}^P_{10}\right][.]\,dV}{\Gamma^P_{10}}, \frac{\int_V \left[\widehat{\boldsymbol{e}}_z \cdot \boldsymbol{B}^P_{10}\right][.]\,dV}{\Gamma^P_{10}} \tag{15}$$

where Γ^P_{10} is defined in eq. (11) and the quantity within square brackets $[.]$ would be the s or z component terms given in Table 5. The ϕ component terms do not make any contribution to the axial dipole. The two terms which make the highest positive contribution to the axial dipole are $B_s \partial u_z/\partial s$ and $B_s \partial u_s/\partial s$. A positive contribution is also noted for the term $B_z \partial u_z/\partial z$. The terms $B_s \partial u_s/\partial s$ and $B_z \partial u_z/\partial z$ are related to the production of current coils in dynamo simulations (Kageyama et al., 2008; Takahashi and Shimizu, 2012). The term $B_s \partial u_z/\partial s$ represents axial field generation due to shear of axial (z) flow in the radial (s) direction. This process would be influential during the growth phase of the nonlinear dynamo, where columnar convection is excited through slow MAC wave motions. In Table 5, the termwise contributions to the dipole in nonlinear simulations are compared with those in a kinematic simulation at $E = 1.2 \times 10^{-5}$ and $Ra = 140$, which also produces an axial dipole. Kinematic simulations at higher Ra do not produce an axial dipole (Sreenivasan and Kar, 2018), and hence cannot be used for comparison with the nonlinear simulations. Even in the absence of slow wave motion, the term $B_s \partial u_z/\partial s$ contributes positively to dipole growth in the kinematic dynamo due to the growth of B_s. Surprisingly, the toroidal–poloidal field conversion via the term $(B_\phi/s)\partial u_s/\partial \phi$ – a dominant process in the kinematic simulation – makes a negative contribution to the dipole in the nonlinear simulation (Table 5). In fact, B^s_{10}, the axial dipole part of the radial field component, is negatively correlated with $(B_\phi/s)\partial u_s/\partial \phi$ in the nonlinear simulation (Fig. 13). The contribution of this term to the overall poloidal field is, however, positive, which suggests that the classical alpha effect (Moffatt, 1978) is still influential

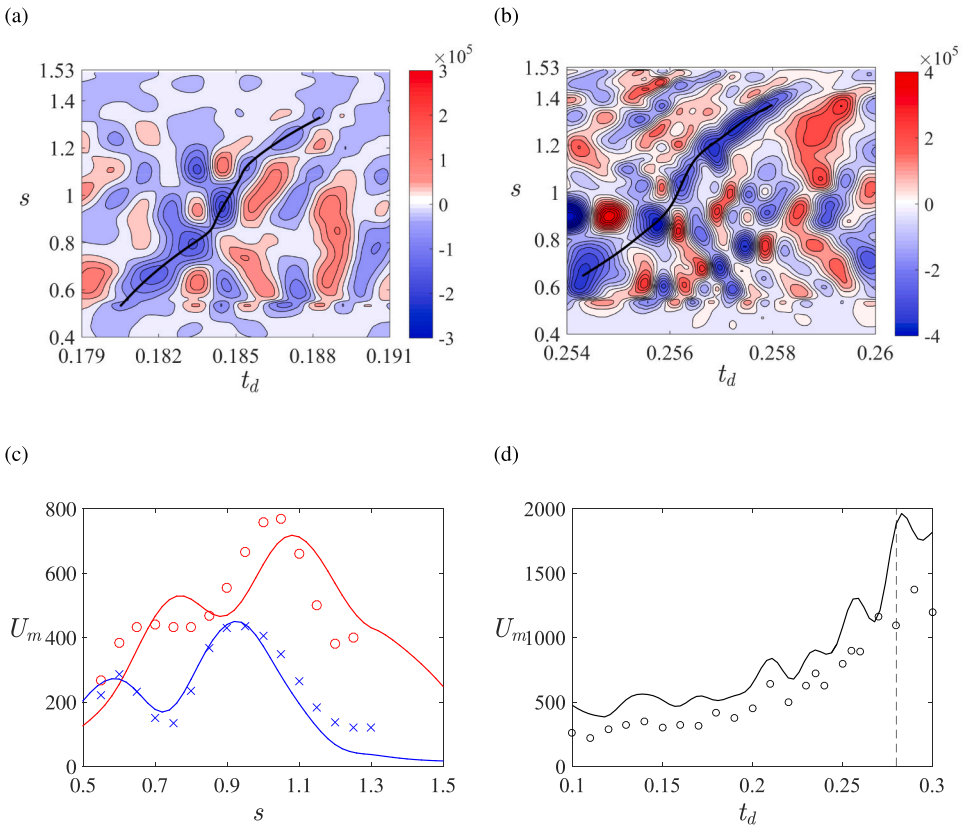

Fig. 12. (a) and (b) Contour plots of z-averaged $\dot{u}_z$ for two time intervals for the large scales $l \leq 31$. The group velocity of the waves is measured from the slope of the black line. (c) Comparison of estimated (theoretical) and measured velocities at each instant of time for the time intervals in (a) and (b), shown in blue and red respectively. The solid line gives the estimated wave velocity and symbols represent the measured values. (d) Comparison of peak velocities measured in the simulations (symbols) with the estimated wave velocity. The group velocity is estimated using the peak value of B_s. The vertical dashed line shows the dipole formation time. The dynamo parameters are $Ra = 400$, $Pm = Pr = 1$, $E = 1.2 \times 10^{-6}$.

Table 5
Relative contribution (in per cent) to the axial dipole by the stretching and advection terms in the magnetic induction equation, calculated from the ratio (15). In the nonlinear simulations, the values are evaluated at a time instant just before dipole formation. The energy-containing range of scales $l \leq l_E$ is considered for the nonlinear simulations while the entire range of scales is considered for the kinematic simulations, marked by the superscript *.

E, Ra	$B_s\partial u_s/\partial s$	$B_s\partial u_z/\partial s$	$B_z\partial u_z/\partial z$	$B_z\partial u_s/\partial z$	$(B_\phi/s)\partial u_z/\partial\phi$	$(B_\phi/s)\partial u_s/\partial\phi$
1.2×10^{-6}, 400	96.90	136.40	14.20	2.60	−49.90	−83.20
1.2×10^{-5}, 220	136.2	56.1	32.10	4.70	−44.10	−57.10
1.2×10^{-5}, 500	48.14	76.72	33.70	−10.41	−23.50	−30.64
1.2×10^{-5}, 2000	65.45	52.20	32.01	−7.53	−25.35	−37.51
$^*1.2\times10^{-5}$, 140	−45.76	131.85	8.23	4.24	−68.12	60.05
E, Ra	$-u_z\partial B_z/\partial z$	$-u_s\partial B_s/\partial s$	$-u_z\partial B_s/\partial z$	$-u_s\partial B_z/\partial s$	$-(u_\phi/s)\partial B_z/\partial\phi$	$-(u_\phi/s)\partial B_s/\partial\phi$
1.2×10^{-6}, 400	9.40	65.9	31.7	9.40	−40.0	−93.50
1.2×10^{-5}, 220	39.90	24.50	34.5	−46.1	−39.4	−40.10
1.2×10^{-5}, 500	35.09	27.74	6.52	−110.7	67.3	−19.11
1.2×10^{-5}, 2000	66.10	38.90	4.58	14.08	−60.42	−42.50
$^*1.2\times10^{-5}$, 140	−10.32	67.13	−15.71	−53.04	75.19	−53.07

in generating the full poloidal field from the toroidal field.

7. Concluding remarks

The formation of the axial dipole field in a planetary dynamo is strongly dependent not only on the rotation of the planet but also the self-generated magnetic field within its core. As suggested by earlier studies (Sreenivasan and Jones, 2011; Sreenivasan and Kar, 2018), the role of the magnetic field in dipole formation is well understood from dynamo models that follow the evolution of the magnetic field from a small seed state. At early times of evolution, the fast MAC waves, whose frequency is close to that of linear inertial waves, are abundantly present. As the field exceeds a threshold, marked by $|\omega_M| > |\omega_A|$, slow MAC waves appear; however, it is only when the field is strong enough to have $|\omega_M/\omega_C| \sim 0.1$ that the slow waves have a dominant presence in the dynamo (Table 3 and Fig. 7(c)). The value of $|\omega_M|$ here must be based on the peak rather than the root mean square value of the field, for the so-called MAC wave window that satisfies the inequality $|\omega_C| > |\omega_M| > |\omega_A|$ does not otherwise exist in the energy-containing scales of the dynamo. A recent study on the evolution of isolated blobs subject to this inequality (Sreenivasan and Maurya, 2021) indicates that the peak Elsasser number,

$$\Lambda \sim \left(\frac{\omega_M^2}{\omega_C\omega_\eta}\right)_0,$$

would likely be $O(10^2)$ for parity between the intensities of fast and slow wave motions. The subscript '0' here refers to the "isotropic" state of the blob that is released into the flow by buoyancy. In other words, the

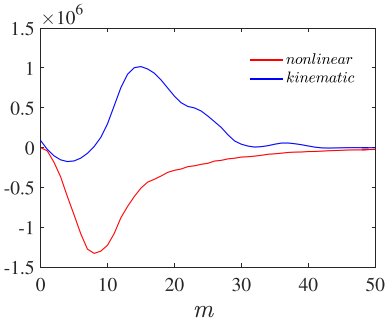

Fig. 13. Spectral distribution of the contribution to the axial dipole energy from the term $(B_\phi/s)\partial u_s/\partial\phi$ for nonlinear and kinematic simulations at $E = 1.2\times10^{-5}$ and $Pm = Pr = 5$. The nonlinear result is obtained from the saturated state at $Ra = 220$ whereas the kinematic result is from a snapshot at $Ra = 140$.

leading-order slow MAC wave frequency ω_s would be $O(10^2)$ times the magnetic diffusion frequency ω_η. The peak value of Λ in simulations at $E \sim 10^{-6}$ vary from $O(10^1)$–$O(10^2)$ as the dynamo field increases towards the saturated state (Fig. 14). The instantaneous value of ω_s/ω_η is higher than Λ due to the anisotropy of the convection as blobs elongate to form columns aligned with the axis of rotation. We anticipate that simulations at lower E would give Λ of $O(10^2)$ for a wider range of $|\omega_M/\omega_C| \sim 0.1$ than in this study. The large peak value of Λ supports the localized excitation of slow magnetostrophic waves at several points in the large scales of spherical harmonic degree $l \le l_E$, even as a global geostrophic balance exists at these scales (e.g. Aurnou and King, 2017). The generation of dynamo helicity – of the same order of magnitude as the nonmagnetic helicity (Fig. 3(a) and (b)) – is consistent with the excitation of the slow waves at these scales. The fact that the large-scale kinetic energy in the dynamo run at $E = 1.2\times10^{-6}$ increases by 90% of its nonmagnetic value suggests that the kinetic energy of the slow MAC wave motions would be of the same order of magnitude as that of the inertial waves.

An interesting aspect of dipole field generation through wave motion is that of poloidal–poloidal field conversion via the term $B_s\partial u_z/\partial s$ in the induction equation. While this term contributes to dipole formation at low Ra in kinematic dynamos through the monotonic increase of B_s, its effect is more pronounced in the nonlinear dynamo over a wide range of Ra, where the generation of radial gradients of u_z happens through the radial propagation of columnar vortices at the Alfvén speed. The

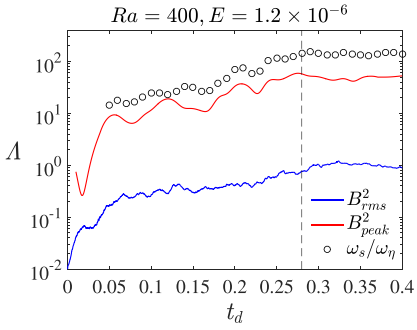

Fig. 14. Peak and volume-averaged (root mean square) values of the Elsasser number $\Lambda = B^2$ shown against magnetic diffusion time, starting from the initial seed field state to the saturated state of the dynamo. The symbols (circles) represent the instantaneous values of ω_s/ω_η, where ω_s is the slow MAC wave frequency and ω_η is the magnetic diffusion frequency. The dashed vertical line marks the dipole formation time. The dynamo simulation has the parameters $Ra = 400$, $Pm = Pr = 1$, $E = 1.2\times10^{-6}$.

twisting of the toroidal field by the radial motion makes a strongly positive contribution to the poloidal dipole field in the kinematic dynamo, whereas it extracts energy from the dipole field in the nonlinear dynamo (Fig. 13).

Since the present study has largely focused on the formation of the axial dipole through magnetostrophic waves, moderately driven dynamos where $|\omega_A| < |\omega_M|$ have been analyzed in detail. This regime is motivated in part by the thermally convecting core of early Earth, which would have produced an axial dipole from a chaotic multipolar field (Sreenivasan and Kar, 2018). The stronger self-generated field that accompanies stronger forcing in numerical dynamos narrows down the MAC wave window in the large scales, although this would not shut down the MAC waves in the rapidly rotating, low-E core. If forcing is so strong that $|\omega_A| \sim |\omega_M|$, then the slow MAC wave frequency would be considerably attenuated. Consequently, the helicity associated with the slow waves would diminish relative to that of the fast waves, which are practically unaffected by the strength of forcing. If geomagnetic reversals are indeed buoyancy-driven (Sreenivasan et al., 2014), then the attenuation of the slow waves should provide a useful constraint on the parameter space that admits reversals.

Supplementary data to this article can be found online at https://doi.org/10.1016/j.pepi.2022.106944.

CRediT authorship contribution statement

Aditya Varma: Methodology, Formal analysis, Investigation, Visualization, Writing – original draft. **Binod Sreenivasan:** Conceptualization, Methodology, Writing – original draft, Writing – review & editing, Supervision, Funding acquisition.

Declaration of Competing Interest

The authors declare that they have no known competing financial interests or personal relationships that could have appeared to influence the work reported in this paper.

Data availability

Data will be made available on request.

Acknowledgments

We thank the editor and the anonymous referees for their thoughtful comments and suggestions, which helped us improve this paper. This study was supported by Research Grant MoE-STARS/STARS-1/504 under Scheme for Transformational and Advanced Research in Sciences awarded by the Ministry of Education, India. The computations were performed on SahasraT, the Cray XC-40 supercomputer at IISc Bangalore.

References

Acheson, D.J., Hide, R., 1973. Hydromagnetics of rotating fluids. Rep. Prog. Phys. 36, 159.
Aubert, J., Finlay, C.C., 2019. Geomagnetic jerks and rapid hydromagnetic waves focusing at earth's core surface. Nat. Geosci. 12 (5), 393–398.
Aubert, J., Gastine, T., Fournier, A., 2017. Spherical convective dynamos in the rapidly rotating asymptotic regime. J. Fluid Mech. 813, 558–593.
Aurnou, J.M., King, E.M., Mar 2017. The cross-over to magnetostrophic convection in planetary dynamo systems. Proc. R. Soc. A. 473 (2199), 20160731.
Bardsley, O.P., Davidson, P.A., 2016. Inertialalfvén waves as columnar helices in planetary cores. J. Fluid Mech. 805, R2.
Braginsky, S.I., 1967. Magnetic waves in the Earth's core. Geomagn. Aeron. 7, 851–859.
Braginsky, S.I., Roberts, P.H., 1995. Equations governing convection in Earth's core and the geodynamo. Geophys. Astrophys. Fluid Dyn. 79, 1–97.
Buffett, B., Bloxham, J., 2002. Energetics of numerical geodynamo models. Geophys. J. Int. 149 (1), 211–224.
Buffett, B., Knezek, N., Holme, R., 2016. Evidence for MAC waves at the top of Earth's core and implications for variations in length of day. Geophys. J. Int. 204 (3), 1789–1800.

Busse, F.H., 1976. Generation of planetary magnetism by convection. Phys. Earth Planet. Inter. 12, 350–358.
Busse, F., Dormy, E., Simitev, R., Soward, A., 2007. Dynamics of rotating fluids. In: Dormy, E., Soward, A.M. (Eds.), Mathematical Aspects of Natural Dynamos, Vol. 13 of The Fluid Mechanics of Astrophysics and Geophysics. CRC Press, pp. 119–198.
Chi-Durn, R., Avery, M.S., Knezek, N., Buffett, B.A., 2020. Decomposition of geomagnetic secular acceleration into traveling waves using complex empirical orthogonal functions. Geophys. Res. Lett. 47 (17) e2020GL087940.
Christensen, U.R., Aubert, J., 2006. Scaling properties of convection-driven dynamos in rotating spherical shells and application to planetary magnetic fields. Geophys. J. Int. 166 (1), 97–114.
Currie, L.K., Tobias, S.M., 2019. Convection-driven kinematic dynamos with a self-consistent shear flow. Geophys. Astrophys. Fluid Dyn. 113 (1–2), 131–148.
Dormy, E., 2016. Strong-field spherical dynamos. J. Fluid Mech. 789, 500–513.
Hori, K., Jones, C.A., Teed, R.J., 2015. Slow magnetic rossby waves in the earth's core. Geophys. Res. Lett. 42 (16), 6622–6629.
Jault, D., 2008. Axial invariance of rapidly varying diffusionless motions in the Earth's core interior. Phys. Earth Planet. Inter. 166, 67–76.
Kageyama, A., Sato, T., 1997. Generation mechanism of a dipole field by a magnetohydrodynamic dynamo. Phys. Rev. E 55 (4), 4617.
Kageyama, A., Miyagoshi, T., Sato, T., Aug 2008. Formation of current coils in geodynamo simulations. Nature 454, 1106–1109.
Kono, M., Roberts, P.H., 2002. Recent geodynamo simulations and observations of the geomagnetic field. Rev. Geophys. 40, 101–113.
Moffatt, H.K., 1978. Magnetic Field Generation in Electrically Conducting Fluids. Cambridge University Press.
Olson, P., Christensen, U., Glatzmaier, G.A., 1999. Numerical modeling of the geodynamo: mechanisms of field generation and equilibration. J. Geophs. Res. Solid Earth 104 (B5), 10383–10404.
Parker, E.N., 1955. Hydromagnetic dynamo models. Astrophys. J. 122, 293.
Penña, D., Amit, H., Pinheiro, K.J., Dec 2018. Deep magnetic field stretching in numerical dynamos. Prog. Earth Planet. Sci. 5 (1), 1–23.
Ponty, Y., Gilbert, A.D., Soward, A.M., 2001. Kinematic dynamo action in large magnetic Reynolds number flows driven by shear and convection. J. Fluid Mech. 435, 261–287.
Ranjan, A., Davidson, P.A., Christensen, U.R., Wicht, J., 2018. Internally driven inertial waves in geodynamo simulations. Geophys. J. Int. 213 (2), 1281–1295.
Ranjan, A., Davidson, P.A., Christensen, U.R., Wicht, J., 2020. On the generation and segregation of helicity in geodynamo simulations. Geophys. J. Int. 221 (2), 741–757.
Roberts, P.H., Zhang, K., 2000. Thermal generation of Alfvén waves in oscillatory magnetoconvection. J. Fluid Mech. 420, 201–223.
Schaeffer, N., Jault, D., Nataf, H.-C., Fournier, A., 2017. Turbulent geodynamo simulations: a leap towards Earth's core. Geophys. J. Int. 211, 1–29.
Sreenivasan, B., Jones, C.A., 2006. The role of inertia in the evolution of spherical dynamos. Geophys. J. Int. 164 (2), 467–476.
Sreenivasan, B., Jones, C.A., 2011. Helicity generation and subcritical behaviour in rapidly rotating dynamos. J. Fluid Mech. 688, 5–30.
Sreenivasan, B., Kar, S., 2018. Scale dependence of kinetic helicity and selection of the axial dipole in rapidly rotating dynamos. Phys. Rev. Fluids 3 (9), 093801.
Sreenivasan, B., Maurya, G., 2021. Evolution of forced magnetohydrodynamic waves in a stratified fluid. J. Fluid Mech. 922, A32.
Sreenivasan, B., Sahoo, S., Dhama, G., 2014. The role of buoyancy in polarity reversals of the geodynamo. Geophys. J. Int. 199, 1698–1708.
Takahashi, F., Shimizu, H., 2012. A detailed analysis of a dynamo mechanism in a rapidly rotating spherical shell. J. Fluid Mech. 701, 228–250.
Teed, R.J., Jones, C.A., Tobias, S.M., 2014. The dynamics and excitation of torsional waves in geodynamo simulations. Geophys. J. Int. 196 (2), 724–735.
Vallis, G.K., 2006. Atmospheric and Oceanic Fluid Dynamics. Cambridge University Press, Cambridge, U.K.
Wicht, J., Christensen, U.R., 2010. Torsional oscillations in dynamo simulations. Geophys. J. Int. 181 (3), 1367–1380.
Willis, A.P., Sreenivasan, B., Gubbins, D., 2007. Thermal core-mantle interaction: exploring regimes for locked' dynamo action. Phys. Earth Planet. Inter. 165, 83–92.